Seventh International Conference on Computational Fluid Dynamics (ICCFD7), Big Island, Hawaii, July 9-13, 2012 **ICCFD7-1303**

Arbitrarily shaped particles in shear flow

M.D. de Tullio*, G. Pascazio* and M. Napolitano*
Corresponding author: m.detullio@poliba.it

* DIMeG and CEMeC, Politecnico di Bari, Italy.

Abstract: Particle motion in shear flow plays an important role in many industrial as well as biomedical applications. In order to study the motion of differently shaped particles within a shear flow, the incompressible Navier–Stokes and the rigid-body-dynamics equations are solved coupled together by means of an implicit iterative approach. An immersed boundary method is used to take into account the presence of moving particles within the fluid domain, without having to regenerate or deform the computational grid. The method has been validated at first by computing flows past a fixed and an oscillating circular cylinder at various values of the Reynolds number (Re). Then, the motion of three differently shaped particles immersed within a low-Re Couette and planar Poiseuille flow has been studied to ascertain their lateral migration and orientation behavior: regardless of their initial position, the neutrally buoyant particles are observed to migrate toward an equilibrium position, depending on the type of the flow. Finally, numerical solutions are presented to understand the influence of increasing Re upon the lateral migration and orientation behavior of the elliptic particle immersed in a Couette flow.

Keywords: Immersed Boundary Method, Fluid-Structure Interaction, Sedimentation, Margination.

1 Introduction

Particle motion in shear flows plays an important role in many industrial applications involving suspension flows, such as transport and refining of oil, paper manufacturing, pharmaceutical processing and environmental waste treatment [1]. The transport of arbitrarily shaped particles is of great importance also in several biomedical applications: particles of various shapes, e. g., spheres, disks and rods [2, 3] have been developed for controlling and improving the systemic administration of therapeutic and contrast agents. Once administered, the particles are transported by the blood along the circulatory system until they reach their targets, their shape playing a crucial role in the phenomenon. Understanding how the shape of the particles influences their lateral migration and orientation within pressure driven flows could help enhancing the design of more effective drugs.

The aim of this work is to develop a numerical tool able to resolve the flow field around arbitrarily shaped particles and to predict their motion when transported by a shear flow, with particular emphasis on the near wall dynamics. In order to achieve such a goal, the immersed boundary (IB) method [4, 5] is more suitable than unstructured body fitted methods, since the governing equations are solved on a fixed structured grid, insofar as it avoids the time-consuming regeneration or deformation of the grid and the successive interpolation of the flow field. Among the various formulations of the IB technique, direct forcing methods [6] are particularly attractive, since they can be easily implemented into existing finite-difference or finite-volume structured solvers. Furthermore, they give very good results for fixed boundaries, also for the compressible Navier–Stokes equations [7, 8], but their extension to fluid-structure-interaction (FSI) problems has been shown to produce oscillatory hydrodynamic forces that are potential source of instabilities [9, 10]. The alternative direct-forcing scheme of Uhlmann [9], computing the forcing on Lagrangian markers (laying on the immersed body) rather than Eulerian points, provides much smoother hydrodynamic forces, with the requirement of a uniform distribution of the Lagrangian markers on the body. Vanella and Balaras [11], improved Uhlmann's approach [9], by using a versatile moving-least-square (MLS) approximation to build the transfer functions between the Eulerian and Lagrangian grids. Their method can handle arbitrary moving and/or deforming bodies, giving accurate results comparable with that of costly alternative methods.

Here, such an approach is used to develop a very efficient numerical tool, based on a second-order-accurate finite-difference fluid solver and on a fully coupled FSI algorithm to deal with the particle dynamics. The solver adopts Cartesian non uniform grids, while the immersed boundaries are described by a triangulation of their surface, independently of the underlying fluid mesh. Firstly, the method has been validated by means of several test cases of increasing complexity: steady and unsteady flows past a fixed circular cylinder at various values of the Reynolds number (Re); flow past a transversely oscillating circular cylinder; flow past an elliptic particle sedimenting in a channel; flow past a a sphere falling under gravity in a fluid-filled box. A good agreement has been obtained in all cases with both experimental and numerical results available in the literature, also when bodies move and the FSI model is involved. Then, the method is used to simulate the transport of single differently shaped particles within unidirectional (in the absence of particles) flows, namely, Couette and plane Poiseuille flows. Only single and two-dimensional particles are considered, for the time being, in order to evaluate the influence of their shape on their lateral migration, and for simplicity.

2 Computational method

The incompressible Navier–Stokes equations are discretized in space using second-order-accurate central differences on a Cartesian staggered grid. The time discretization uses an explicit Adams–Bashforth scheme for the non-linear terms and an implicit Crank–Nicolson scheme for the viscous ones:

$$\frac{\hat{\boldsymbol{u}} - \boldsymbol{u}^n}{\Delta t} = -\alpha \boldsymbol{\nabla} p^n + \gamma\, H^n + \rho\, H^{n-1} + \frac{\alpha}{2\,Re}\, \nabla^2 \left(\hat{\boldsymbol{u}} + \boldsymbol{u}^n \right), \tag{1}$$

where $\boldsymbol{u}^n$ denotes the velocity at the old time n, $\hat{\boldsymbol{u}}$ is the intermediate solution, Δt is the time step, H contains the non-linear terms and α, γ and ρ are the constants of the Adams–Bashforth/Crank–Nicolson scheme [12]. The resulting system is solved using a fractional-step method to obtain the intermediate non-solenoidal velocity field $\hat{\boldsymbol{u}}$. In order to get a divergence-free velocity field, a scalar quantity φ is introduced such that:

$$\boldsymbol{u}^{n+1} = \hat{\boldsymbol{u}} - \alpha\, \Delta t\, \boldsymbol{\nabla} \varphi \tag{2}$$

By applying the discrete divergence operator to the equation above, an elliptic equation for φ is obtained:

$$\nabla^2 \varphi = \frac{\boldsymbol{\nabla} \cdot \hat{\boldsymbol{u}}}{\alpha\, \Delta t} \tag{3}$$

The large-banded matrix associated with the elliptic equation is reduced to a penta-diagonal matrix using trigonometric expansions (FFTs) in the spanwise direction, and the resulting Helmholtz equations are then inverted using the FISHPACK package [13]. Finally, the pressure field is computed as

$$p^{n+1} = p^n + \varphi - \frac{\alpha\, \Delta t}{2\,Re}\, \nabla^2 \varphi \tag{4}$$

In order to overcome the presence of large fluctuations in the pressure and velocity fields arising when using the linear interpolation forcing of Fadlun et al. [6], the MLS approximation of Vanella and Balaras [11] is employed. On the basis of the alternative direct-forcing scheme suggested by Uhlmann [9], the forcing is computed on the Lagrangian markers laying on the immersed surface, so as to satisfy the boundary condition, and then transferred to the Eulerian grid-points. The MLS approximation was the key ingredient to build a transfer functions between the Eulerian and Lagrangian grids, that is able to provide a smooth solution also in the presence of arbitrarily moving/deforming bodies. The reconstruction procedure consists of the following steps:

1. Compute the intermediate velocity $\hat{\boldsymbol{u}}$ from equation (1) in all the ne Eulerian grid points surrounding a Lagrangian point in its support domain. Here, the support domain is centered on the Lagrangian point, and extends over $\pm 1.6 \Delta x_i$, where Δx_i is the local grid size in the $i-th$ direction. In this way, 9 and 27 Eulerian points are considered in two and three dimensions, respectively.

2. Compute the velocity at all the Lagrangian grid points corresponding to the non-solenoidal velocity field:

$$\hat{\boldsymbol{U}}(\boldsymbol{x}) = \sum_{k=1}^{ne} \phi_k^l(\boldsymbol{x})\, \hat{\boldsymbol{u}}_k \tag{5}$$

where ϕ is the transfer operator containing the shape functions and obtained minimizing with respect to $\boldsymbol{a}(\boldsymbol{x})$ the weighted L2-norm defined as:

$$J = \sum_{k=1}^{ne} W(\boldsymbol{x} - \boldsymbol{x}^k) \left[\boldsymbol{p}^T(\boldsymbol{x}^k)\, \boldsymbol{a}(\boldsymbol{x}) - \hat{\boldsymbol{u}}_k\right]^2 \;;$$

in the above equation, $\boldsymbol{p}^T(\boldsymbol{x})$ is the basis function vector, $\boldsymbol{a}(\boldsymbol{x})$ is a vector of coefficients, $\boldsymbol{x}$ is the Lagrangian grid-point position, and $W(\boldsymbol{x} - \boldsymbol{x}^k)$ is a given weight function. The exponential function is used that can be written as:

$$W(\boldsymbol{x} - \boldsymbol{x}^k) = \begin{cases} e^{-(r_k/\alpha)^2} & r_k \le 1 \\ 0 & r_k > 1 \end{cases} \tag{6}$$

where $\alpha = 0.3$ and r_k is given by

$$r_k = \frac{|\boldsymbol{x} - \boldsymbol{x}^k|}{r_w} \tag{7}$$

r_w being the size of the support domain.

3. Calculate the volume force $\boldsymbol{F}$ at all Lagrangian grid points, in order to get the desired velocity $\boldsymbol{U}_b$ at the boundary:

$$\boldsymbol{F} = \frac{\boldsymbol{U}_b - \hat{\boldsymbol{U}}}{\Delta t} \tag{8}$$

4. Transfer $\boldsymbol{F}$ to the k Eulerian grid points associated with each Lagrangian grid point, using the same shape functions used in the interpolation procedure, properly scaled by a factor c_l, which is determined by imposing that the total force acting on the fluid is not changed by the transfer:

$$\boldsymbol{f}^k = \sum_{l=1}^{nl} c_l\, \phi_k^l \boldsymbol{F}_l; \tag{9}$$

nl indicates the number of Lagrangian points associated with the Eulerian point k. One can also verify that the above scheme guarantees the equivalence of total torque between the Eulerian and Lagrangian computational grids [11].

5. Correct the intermediate velocity by means of the forcing, so as to satisfy the boundary conditions at the immersed body:

$$\boldsymbol{u}^* = \hat{\boldsymbol{u}} + \Delta t\, \boldsymbol{f}; \tag{10}$$

this velocity field is not divergence-free and is projected into a divergence-free space by applying the pressure correction which satisfies the Poisson equation (3).

The forces and moments acting on the immersed body are calculated in time by integrating the pressure and viscous stresses over the immersed body surface. Given the surface discretization by nl triangular elements, one has:

$$\boldsymbol{F}_{tot}(t) = \sum_{l=1}^{nl} (\boldsymbol{\tau}_l \cdot \boldsymbol{n}_l - p_l \boldsymbol{n}_l)\, S_l \qquad \boldsymbol{M}_{tot}(t) = \sum_{l=1}^{nl} [\boldsymbol{r}_l \times (\boldsymbol{\tau}_l \cdot \boldsymbol{n}_l - p_l \boldsymbol{n}_l)]\, S_l \tag{11}$$

where $\boldsymbol{\tau}_l$ and p_l are the viscous stress tensor and pressure, evaluated at the centroid of each triangle (location of the Lagrangian marker, l), while $\boldsymbol{r}_l$ is the distance of the Lagrangian point from the centroid of the body, $\boldsymbol{n}_l$ and S_l are the normal unit vector and area of each triangle. In order to evaluate the pressure p_l and the velocity derivatives, $(\partial u_i/\partial x_j)_l$ needed for the viscous stress tensor, for each Lagrangian marker a probe is created along its normal direction, at a distance h_l, equal to the averaged local grid size. Using the same MLS formulation described above, the pressure and velocity are evaluated on the probe location. Then, the pressure on the markers is calculated as:

$$p_l = p_l^p + \frac{D\boldsymbol{v}_l}{Dt} \cdot \boldsymbol{n}_l \tag{12}$$

where p_l^p is the pressure at the probe and the second term of the right hand side takes into account the acceleration of the marker, $D\boldsymbol{v}_l/Dt$ [10]. Concerning the velocity derivatives on the body surface, these are considered equal to the velocity derivatives evaluated at the probe. This is equivalent to assume a linear variation of the velocity near the body, a good approximation provided that the grid is sufficiently refined near the body.

The evaluation of the flow and particle motion at each time step is carried out by a strongly coupling scheme, since the prediction of the flow field and of the hydrodynamic loads requires the knowledge of the motion of the bodies and vice–versa. An iterative implicit approach in considered, as reported in de Tullio et al. [14]: for each time step, the convergence of the iterative procedure is verified by the condition $\mid \boldsymbol{v}_p^j - \boldsymbol{v}_p^{j-1} \mid < \epsilon$, where $\boldsymbol{v}_p^j$ indicates the body angular and linear velocities at iteration j. In all our computations a tolerance of $\epsilon = 10^{-6}$ was used and the number of iterations required for convergence at each time step varied from 1 to 6, depending on the flow configuration. In order to avoid numerical instabilities in the FSI algorithm induced by the added mass effect, an under–relaxation of the forces (and moments) is employed, according to $\boldsymbol{F}_{tot} = \gamma \boldsymbol{F}_{tot}^j + (1-\gamma)\boldsymbol{F}_{tot}^{j-1}$ with $\gamma = 0.9$.

3 Results

Several test cases of increasing complexity are considered in order to validate the method and to show its accuracy: a fixed circular cylinder in steady and unsteady conditions, a circular cylinder transversely oscillating in a cross-flow with prescribed motion, an elliptic particle sedimenting in a confined channel, and a sphere falling under gravity in a box. The results are compared with experiments and other numerical results available in the literature. In the final part of the section the results of the transport of single differently shaped particles in shear flows is provided.

3.1 Fixed circular cylinder

The case of the flow past a fixed circular cylinder is considered at first in order to validate the method. Four values of the Reynolds number, based on the cylinder diameter D and the free-stream velocity U, are considered, namely, 20, 40, 100, and 200. The first two cases correspond to steady flow regimes and the last two to unsteady ones. The computational domain is $[-10D, 40D] \times [-20D, 20D]$. Inlet and outlet boundary conditions are imposed on the vertical boundaries, while free-shear wall conditions are imposed for the horizontal boundaries. A non uniform grid of 800×700 nodes is used with a uniform grid spacing of $0.01D$ in the vicinity of the cylinder. The Lagrangian markers are distributed uniformly onto the cylinder surface, with a spacing of $0.007D$, that is equal to 0.7 the local Eulerian grid size in that area. The constant time step used is $\Delta t = 0.001\, D/U$. The length of the recirculating zone, L, the streamwise distance from the cylinder back to the center of one vortex, a, the gap between the centers of the two vortices, b, appropriately non-dimensionalized by the cylinder diameter, as well as the the drag coefficient, C_D, for the two steady cases, are provided in Table 1. The time histories of the viscous and pressure forces in the two Cartesian directions for the case $Re = 100$ are given in Figure 1, while the computed drag and lift coefficients, C_D and C_L, and Strouhal number, St, are reported in Table 2 for the two unsteady cases. Other numerical and experimental results available in the literature are provided in the tables for reference, showing a good agreement.

	Re=20				Re=40			
	L	a	b	C_D	L	a	b	C_D
Coutanceau and Bouard [15]	0.93	0.33	0.46	–	2.13	0.76	0.59	–
Tritton [16]	–	–	–	2.09	–	–	–	1.59
Linnick and Fasel [17]	0.93	0.36	0.43	2.06	2.28	0.72	0.60	1.54
Taira and Colonius [18]	0.94	0.37	0.43	2-06	2.30	0.73	0.60	1.54
de Palma et al. [7]	0.93	0.36	0.43	2.05	2.28	0.72	0.60	1.55
present	0.95	0.37	0.42	2.20	2.30	0.75	0.60	1.60

Table 1: Non-dimensional length of the recirculating zone, L, streamwise distance from the cylinder back to the center of one vortex, a, gap between the centers of the two vortices, b, and drag coefficient, C_D, for the steady flow past a circular cylinder at $Re = 20$ and $Re = 40$. References [15],[16] provide experimental results, while the others are numerical results obtained with different implementations of non-body conformal methods.

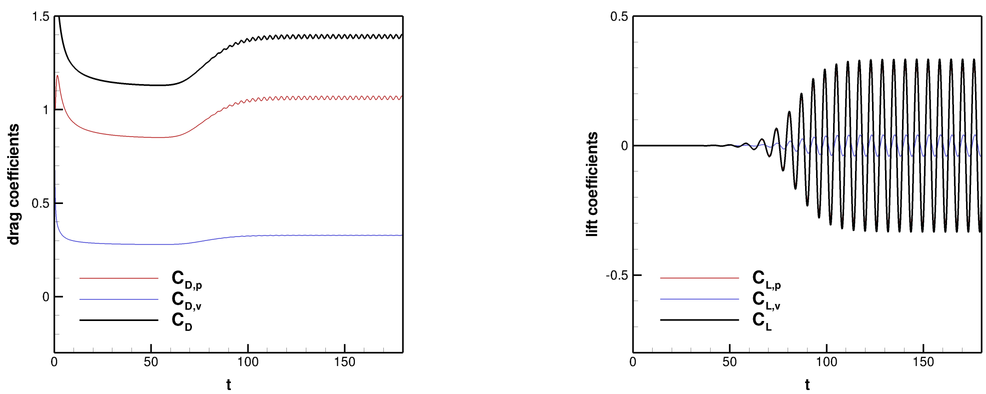

Figure 1: Time histories of the force coefficients for the flow past a circular cylinder at $Re = 100$. $C_{D,p}$ and $C_{L,p}$ are the pressure drag and lift coefficients respectively, while $C_{D,v}$ and $C_{L,v}$ are the drag and lift coefficients due to viscous forces, respectively.

3.2 Oscillating circular cylinder in a cross-flow

The case of a circular cylinder transversely oscillating in a cross-flow is considered in order to validate the method in case of a moving geometry with a prescribed motion. As showed by Uhlmann [9], in this case the direct forcing approach of Fadlun et al. [6], can lead to large fluctuations of the hydrodynamic forces. The Reynolds number, based on the cylinder diameter D and the free-stream velocity U, is equal to 185. Two values of the ratio between the forcing frequency, f_e, and the natural shedding frequency, f_0, are considered, namely, 1 and 1.2, with $f_0 D/U = 0.195$. The motion of the cylinder is given by $y(t) = A_0 sin(2\pi f_e t)$, with $A_0 = 0.2D$. The same computational grid used for the fixed cylinder case is used, as well as the same Lagrangian markers distribution and spacing. The constant time step used is $\Delta t = 0.001\, D/U$. The time histories of the lift and drag coefficients for the two cases are reported in Figure 2. The different behavior of the force coefficients is captured accurately, and the results are in very good agreement with those obtained by Vanella and Balaras [11], using a similar approach, and with those of Guilmineau and Queutey [21], obtained using a body-fitted approach. A comparison between the drag coefficient obtained by the present method and that obtained using the same simulations parameters but using the direct forcing of Fadlun et al. [6] is provided in Figure 3. It is interesting to note that the anomalous oscillations of the force are smoothed out by the the MLS formulation. Finally, the distribution of pressure and skin-friction coefficients, C_p and C_f, respectively, on the cylinder surface are shown in Figure 3, at the time instant corresponding to the extreme upper position, compared with the results of Guilmineau and Queutey [21]. The agreement is

	Re=100			Re=200		
	C_D	C_L	St	C_D	C_L	St
Berger and Willie [19]	–	–	0.16 - 0.17	–	–	0.18 - 0.19
Linnick and Fasel [17]	1.34 ± 0.009	± 0.333	0.166	1.34 ± 0.044	± 0.69	0.197
Taira and Colonius [18]	–	–	–	1.35 ± 0.048	± 0.68	0.196
de Palma et al. [7]	1.32 ± 0.010	± 0.331	0.163	1.34 ± 0.045	± 0.68	0.190
Le et al. [20]	1.37 ± 0.009	± 0.323	0.160	–	–	–
present	1.39 ± 0.010	± 0.331	0.168	1.39 ± 0.049	± 0.684	0.200

Table 2: Force coefficients and Strouhal number for the unsteady flow past a circular cylinder at $Re = 100$ and $Re = 200$. Reference [19] provides experimental results, while the others are numerical results obtained with different implementations of non-body conformal methods.

good and the smoothness of the local forces coefficients is clear.

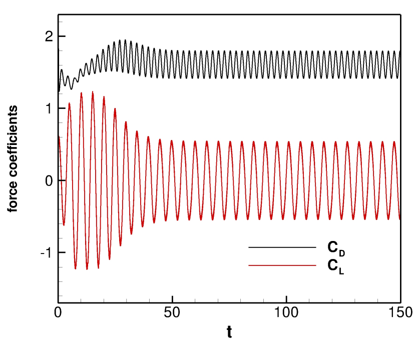

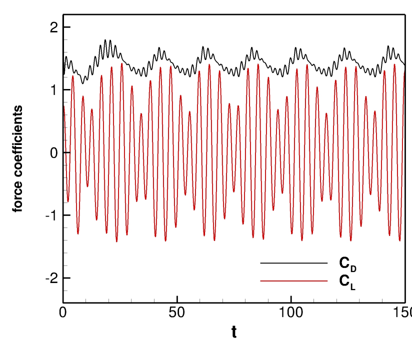

Figure 2: Force coefficients as a function of time for the case of a cylinder oscillating in a cross-flow, $f_e/f_0 = 1.0$ (left) and $f_e/f_0 = 1.2$ (right)

.

3.3 Sedimentation of an elliptic particle

The dynamics of a single elliptic particle sedimenting in a confined channel is considered here to validate the FSI procedure. In Figure 4 the geometrical parameters of the problem are reported. The aspect ratio, $\alpha = a/b$, where a and b are the major and minor axes, respectively, is set equal to 2, while the blockage ratio is set equal to $\beta = L/a = 4$, being L the width of the channel. The density ratio, $\gamma = \rho_s/\rho_f = 1.1$, where ρ_s and ρ_f are the particle and fluid densities, respectively. Considering the terminal settling velocity of the particle, U_t, the major axis of the ellipse and the fluid kinematic viscosity, ν, the Reynolds number is $Re_t = U_t a/\nu = 12.5$, while the Froude number is $Fr_t = U_t/\sqrt{ga} = 0.126$, where g is the gravity acceleration. The computational domain is $[0, L] \times [0, 7L]$. The particle starts falling with the centroid in $(0.5L, 6L)$, with an initial angle of $\theta_0 = \pi/4$, to break the symmetry. No-slip wall conditions are imposed on the vertical boundaries of the domain, while no-flow conditions are imposed on the horizontal boundaries. A uniform grid of 301×2101 nodes is used with a grid spacing of $0.013a$. The Lagrangian markers are distributed uniformly onto the particle surface, with a spacing of $0.01a$, that is equal to 0.77 the Eulerian grid size. The constant time step used is $\Delta t = 0.001\, a/U_t$. In Figures 4 and 5 the present results in terms of particle settling velocity, trajectory (location of center of mass) and orientation are compared with the numerical results obtained by Xia et al. [22] by means of a finite-element method. The particle settles into the center of the channel ($x/L = 0.5$) with a constant velocity, and sediments in a horizontal configuration ($\theta/\pi = 0$). The agreement of the results is very good.

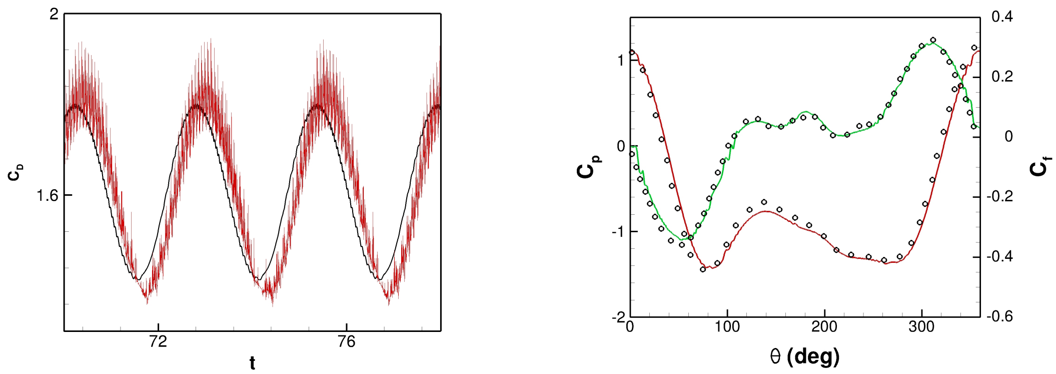

Figure 3: Left: comparison between the drag coefficient calculated using the present method (black line) and that obtained using the forcing of Fadlun et al. [6]. Right: pressure (red line) and skin friction (green line) coefficients, C_p and C_f for the case of a cylinder oscillating in a cross-flow, $f_e/f_0 = 1.0$, when it is located at the extreme upper position. Continuous lines indicate the present results, while symbols indicate the results obtained by body-fitted simulations by Guilmineau and Queutey [21].

3.4 Single sphere settling under gravity

To further validate the method, a three-dimensional case involving fluid-structure interaction is considered, by simulating the motion of a sphere falling under gravity in a closed container. The group of ten Cate et al. [23] performed experimental investigations by means of particle image velocimetry, providing an accurate measure of both the sphere trajectory and velocity from the moment of its release until rest at the bottom of the channel. Given the relative small ratio between the box width and the particle diameter, the full flow field can be simulated under identical conditions. The Froude and Reynolds number are defined using the sphere diameter, d, and the sedimentation velocity of a sphere in an infinite medium, u_∞. In order to determine u_∞, the relation for the drag coefficient of Abraham [24] is used:

$$C_d = C_0 \left(1 + \frac{\delta_0}{\sqrt{Re}}\right)^2 \tag{13}$$

with $C_0\delta_0^2 = 24$ and $\delta_0 = 9.06$. Four different conditions are considered, with different density ratios, γ, and parameters, as reported in Table 3. The computational domain considered is $[0, 6.67d] \times [0, 6.67d] \times$

Re_∞	γ	u_∞ (m/s)	Fr_∞	$\Delta t\, u_\infty/d$
1.5	1.155	0.038	0.0991	0.0001
4.1	1.161	0.060	0.156	0.0005
11.6	1.164	0.091	0.237	0.0007
31.2	1.167	0.128	0.334	0.001

Table 3: Reynolds number, density ratio, settling velocity in an infinite medium, Froude number and non-dimensional time step used in the simulation for the case of a sphere settling under gravity in a closed channel.

$[0, 10.67d]$, where the last is the gravity acceleration direction. The particle starts falling with the centroid in $(3.33d, 3.33d, 8d)$. No-slip wall conditions are imposed on the vertical boundaries of the domain, while no-flow conditions are imposed on the horizontal boundaries. A uniform grid of $241 \times 241 \times 385$ nodes is used with a grid spacing of about $0.028d$. The Lagrangian markers are distributed uniformly onto the sphere surface, with a spacing of $0.02d$, that is equal to 0.71 the Eulerian grid size. The constant time step used depends on the case considered and is reported in Table 3. The sphere sedimentation velocity and trajectory

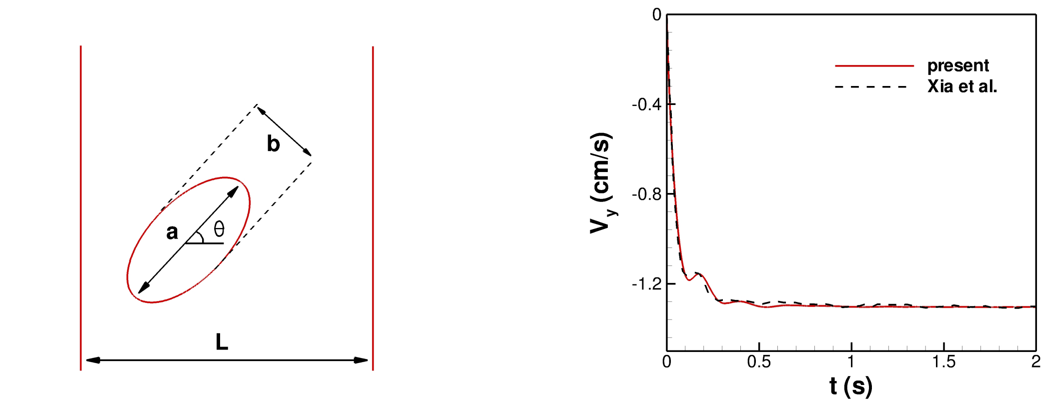

Figure 4: Geometrical parameters for the elliptic particle sedimenting in a confined channel (left) and sedimentation velocity (right). Present numerical results (continuous line) are compared with the numerical results of Xia et al. [22] (dashed line).

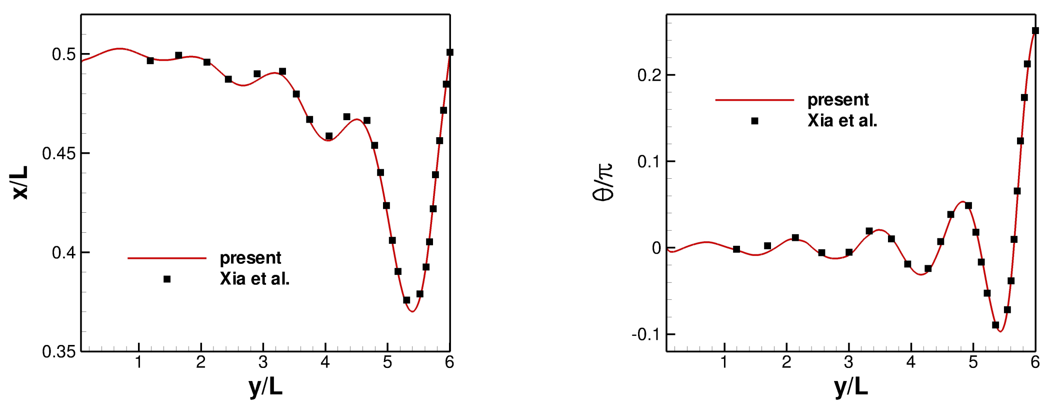

Figure 5: Particle trajectory (location of center of mass) and orientation for the elliptic particle sedimenting in a confined channel. Present numerical results (lines) are compared with the numerical results obtained by Xia et al. [22] by means of a finite-element method (symbols).

are reported in Figure 6, where the present results are compared with the experimental data given in [23]. A very good agreement is obtained for all the configurations considered.

3.5 Transport of differently shaped single particles

The two-dimensional motion of a single particle, in an infinite channel is considered, in order to study its lateral migration in shear flows and the influence of the particle shape. Feng et al. [25, 26] simulated the motion of a single circular particle in planar Couette and Poiseuille flow using a finite element method. The difference in the relative velocity across a solid particle may drive it to move laterally since the side with a higher relative velocity may lead to a lower pressure. Therefore, they suggested that four mechanisms are responsible for the motion in shear flows: wall lubrication repulsion; inertial lift due to shear slip; lift due to particle rotation; lift associated with the curvature of the undisturbed velocity profile (for the case of Poiseuille flow).

The reference particle considered here is the circular one, with diameter d. The channel height is $h = 4d$. The computational domain is $[-50d, 50d] \times [0, 4d]$, with periodic boundary conditions in the horizontal direction. In the vertical direction, no-slip wall is imposed at the lower surface of the domain, while the

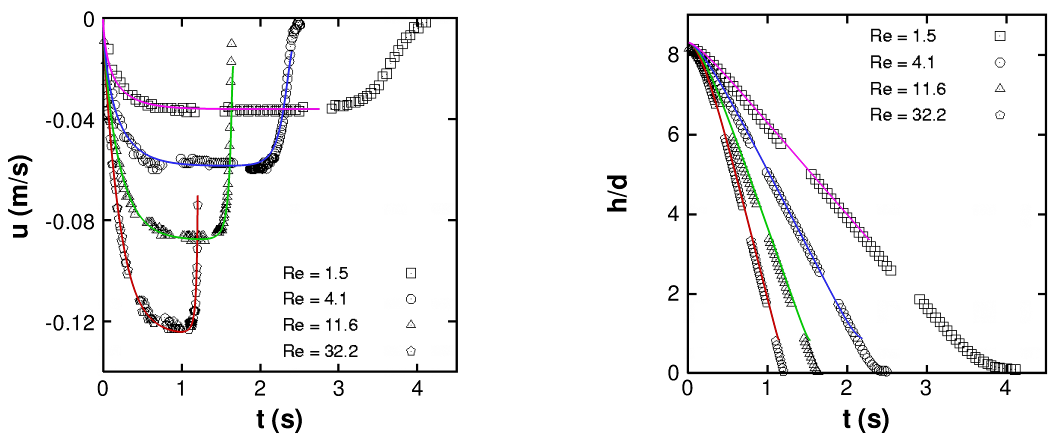

Figure 6: Numerical results (continuous lines) of the sphere sedimentation velocity and trajectory compared with experimental results (symbols) of ten Cate et al. [23] at four Reynolds numbers.

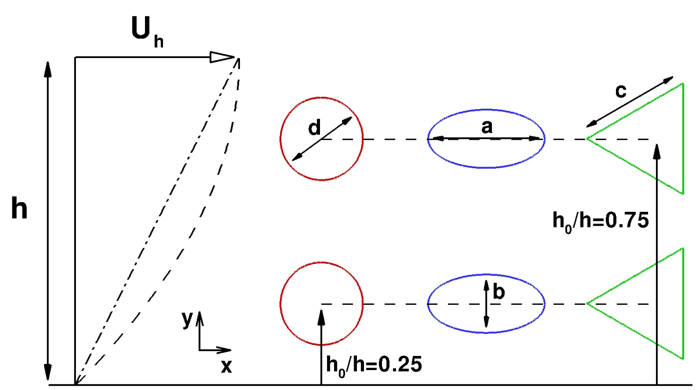

h

Figure 7: Relevant geometrical quantities for the transport of a differently shaped particle.

upper surface has an imposed velocity, U_h. Three neutrally buoyant particles of different shape and equal area are considered (see Figure 7): a circle, an ellipse, with a and b major and minor axes respectively and $a/b = 2$, and an equilateral triangle, with side c. The particles are released in the channel at two different initial positions, h_0/h, equal to 0.25 (close to the wall) and 0.75 (close to the upper surface), with an orientation with respect to the horizontal direction as shown in Figure 7. The Reynolds number considered, Re, based on the reference length, d, the upper surface velocity U_h and the fluid kinematic viscosity, is equal to 20, in order to include inertial effects in the phenomenon. The two flow configurations considered are characterized by unidirectional flow in the absence of the particle. The first one is the case of null pressure gradient in the streamwise direction, giving a Couette flow, with a linear velocity profile, when the particle is absent; the second one is the case with a negative pressure gradient in the flow direction, so as to have a plane-Poiseuille quadratic velocity profile when the particle is absent. In all cases, the particles are first considered fixed, with their centroid at a distance h_0/h from the wall, for a non-dimensional time of $t_{fixed}U_h/d = 10$, under the shear flows. After that, the particles are released and start translating and rotating in the channel. A uniform grid of 5000×200 nodes is used with a uniform grid spacing of $0.02d$. The Lagrangian markers are distributed uniformly onto the particle surface, with a spacing of $0.014d$, that is equal to 0.7 the local Eulerian grid size in that area. The constant time step used is $\Delta t = 0.005\, d/U_h$.

Ho and Leal [27] and later Vasseur and Cox [28] show that in conditions of low Reynolds number, neutrally

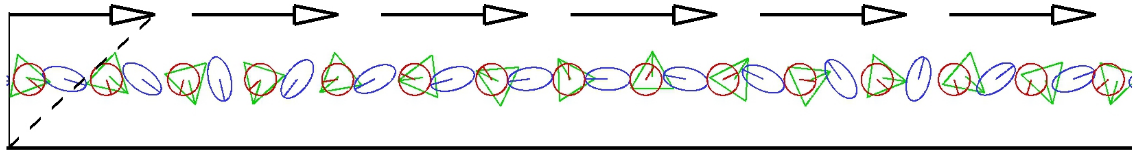

Figure 8: Example of equilibrium particle position for the case of $Re = 20$ and linear velocity profile.

buoyant particles in a simple shear Couette flow will migrate toward the center plane because of the influence of the walls (agreeing with experimental observations by Halow and Wills [29]). In the present simulations for the Couette flow, the particles are observed to migrate toward the median plane of the channel, as shown in Figure 8, regardless of their initial position and shape. The same results are obtained by Feng et al. [26] for the cylindrical particle. Note that the migration velocity of the particles depends on the initial conditions at the early migration stage. In [26] the particles start moving with the same fluid velocity at their initial position, so that the time history of their results is different from the one presented here. Despite these differences, the trends are alike. Figure 9 reports the particle vertical position, horizontal velocity and angular velocity versus horizontal position, for the three particles. The cylindrical particle starting away from the wall migrates rapidly toward the equilibrium position, while the one starting in the vicinity of the wall reaches the same position more gradually. The ellipsoidal particle has the same behavior. The triangular particle starting away from the wall rapidly migrates toward the wall, until the wall repulsion pushes the particle toward the middle of the channel, as in the case of the particle starting near the wall. It is worth noting that the centroid positions of the ellipsoidal and triangular particles exhibit a periodic behavior, with a mean value that coincides with the middle of the channel. As indicated in Figure 9 (middle), the particles have a translational velocity equal to that corresponding to the undisturbed flow in the same position (indicated by a green dashed line in the figure), where for the case of the ellipsoidal and triangular particles the mean velocity is intended. All the three particles rotate, with an instantaneous angular velocity that depends on the geometry: a constant value is obtained for the circular particle, while periodic behavior is observed for the other two. On the other hand, the mean value of the angular velocity for the ellipse and the triangle, is almost equal to that of the cylinder, that is about the 47% of the constant shear rate of the undisturbed flow field. This means that the particles rotate with the angular velocity of the flow field to within a small correction, as found also by Feng et al. [26] for the cylindrical particle.

Segré and Silberberg [30, 31] studied the behavior of a neutrally buoyant ridig sphere in pipe flow by means of experiments. They showed that solid particles migrate across streamlines in the presence of walls, velocity profile curvature and buoyancy forces, unless the particle is so small that its relative motion with respect to the fluid is negligible [32]. They also found that a neutrally buoyant particle will migrate to an equilibrium position at about 60% from the center plane to the walls, in conditions of small but finite Reynolds number. The effect was called the *tubular pinch effect*, because of the tube-like shape of the annular region to which particles migrate. This was the first quantitative experimental evidence of lateral migration of a sphere in unidirectional pipe flow of Newtonian fluid. In this work, two-dimensional conditions are considered, so that, as indicated by Feng et al. [26], many features of the results of the present simulations apply qualitatively to three-dimensional experiments, but quantitative comparisons are imperfect. In our simulations, for the plane Poiseuille flow, there is in general a competition between inward and outward forces, leading to an equilibrium position between the wall and the mid-channel, as shown in Figure 10. The equilibrium position is reached regardless of the particle initial position, while the equilibrium position is slightly dependent on the particle shape. The ellipse and triangle positions have an oscillatory behavior around a mean value. The particles starting near the wall have a monotone behavior of the margination velocity, moving toward the equilibrium position that is away from the wall. Particles starting away from the wall, on the other hand, initially migrate rapidly toward the wall, reaching a position (closer to the wall than the equilibrium position) where the wall repulsive force inverts the sign of their margination velocity, and then reach equilibrium. It is interesting to note that, as indicated in Figure 10 (middle), considering the average value of the particle translational velocity for the ellipse and the triangle, all the particles always lag the local velocity of the undisturbed flow (indicated by a green dashed line in the figure). This result was also

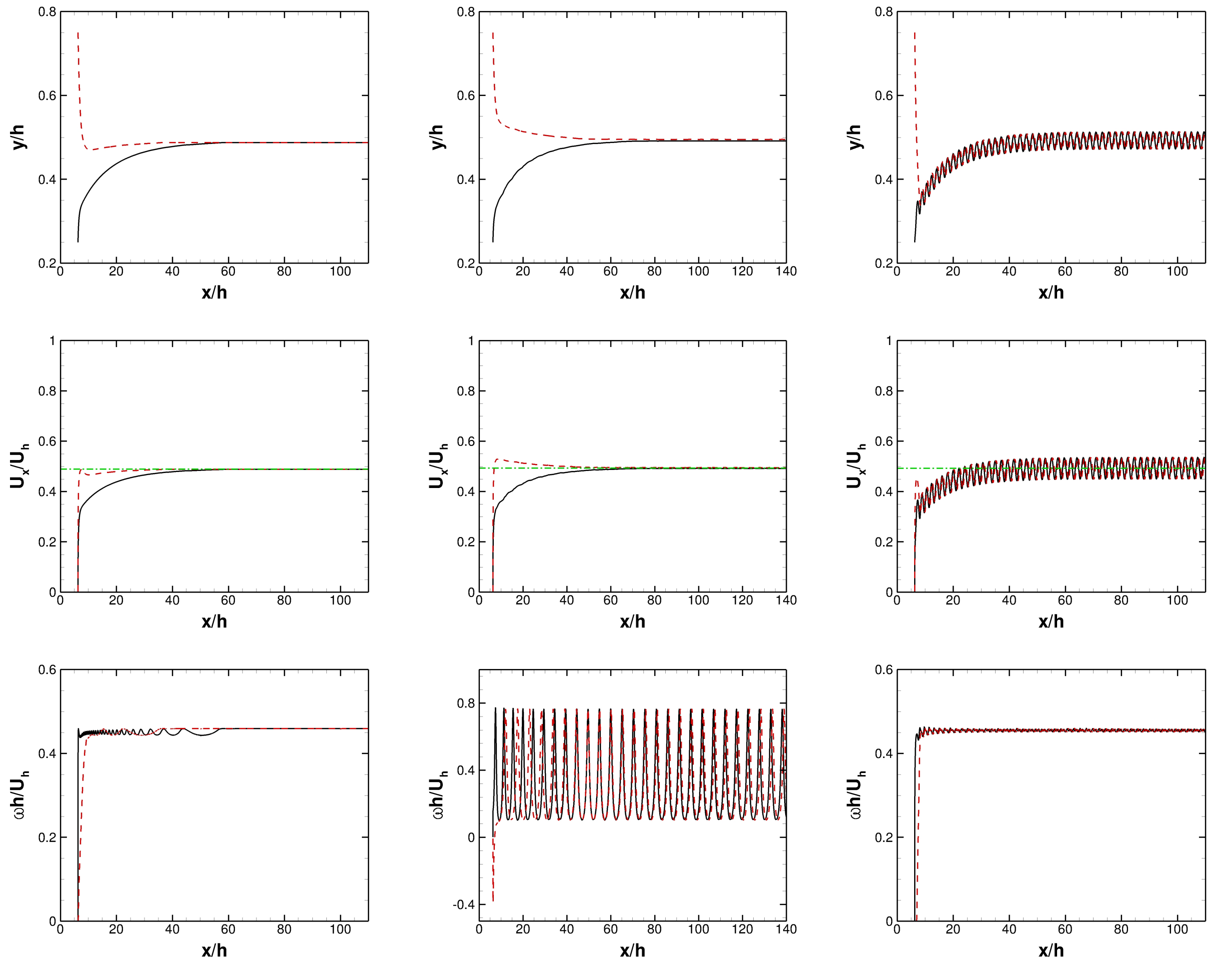

Figure 9: Particle vertical position (top), horizontal velocity (middle) and angular velocity (bottom) versus horizontal position for the case of $Re = 20$ and Couette flow. From left to right: cylinder, ellipse and triangle.

found by Feng et al. [26] for the cylindrical particle, and is a well known effect in the limit of small particles in slow flows [33]. All the three particles rotate, with an instantaneous angular velocity that depends on the geometry. If we consider the mean values of the angular velocity for the ellipse and the triangle, all the particles have the same value, within a small correction, that is about the 47% of local shear rate of the undisturbed flow field.

In order to study the effect of the Reynolds number on the margination of particles, we concentrate our attention to the case of the elliptic particle in Couette flow, at increasing Reynolds numbers. The angle θ between the ellipse major axis and the horizontal direction is zero when the particle is released. Figure 11 reports the vertical position and θ/π versus horizontal position for some of the cases examined. Each single elliptic particle migrates to the equilibrium position, which moves closer to the wall as the Reynolds number increases. This final position is independent of the initial position (here only the results for $h_0/h = 0.75$ are reported). For the lower Reynolds numbers, particles always rotate, even when they are in the equilibrium position, due to the applied shear force.

The behavior of θ is due to an angular velocity that is periodic in time, showing spikes to reach the maximum value (not reported here; see Figure 9 for the case of $Re = 20$). In fact, as Re increases the rotation of the particle is delayed, as shown in Figure 11 (right): the particle remains with an almost fixed orientation with respect to the flow direction, and periodically experiences a 180° rotation, with period increasing with Re. An interesting result for this particular case is found for $Re > 77.5$ in our simulations,

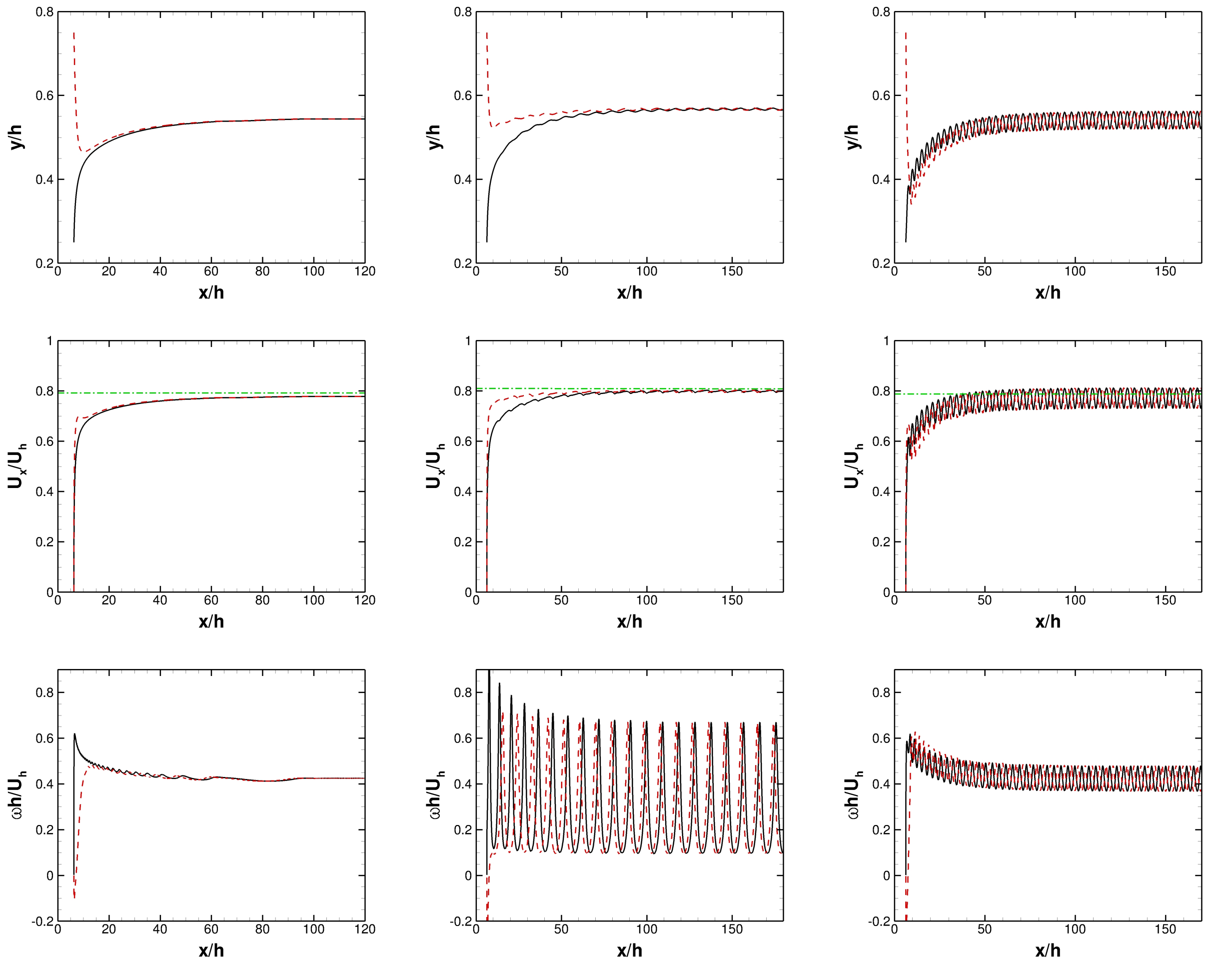

Figure 10: Particle vertical position (top), horizontal velocity (middle) and angular velocity (bottom) versus horizontal position for the case of $Re = 20$ and plane Poiseuille flow. From left to right: cylinder, ellipse and triangle.

with the particle that exhibits no rotation: the particle remains at a fixed orientation with respect to the current.

4 Conclusion and Future Work

This paper provides a numerical tool under development, which aims at resolving the flow field around particles transported in shear flows, namely, a second-order-accurate finite difference fluid solver, coupled with an implicit fluid-structure-interaction algorithm to deal with the fluid and particle dynamics. A suitable immersed boundary method based on a moving-least-square approximation is employed, able to handle arbitrary moving and/or deforming bodies and to obtain accurate and smooth hydrodynamic forces. The method has been validated by means of several test cases of increasing complexity, involving flows past fixed bodies, moving bodies with prescribed motion and bodies falling inside a fluid, so that fluid-structure-interaction is also involved. A very good agreement has been obtained with experimental as well as numerical results available in the literature. The transport of neutrally buoyant single particles in Couette and planar Poiseuille flows, at small Reynolds number, is then presented. Three particles having identical area and different shapes, namely, a circle, an ellipse and a triangle, have been considered so as to analyze the influence of their shape on their lateral migration. The particles are observed to migrate toward an equilibrium position

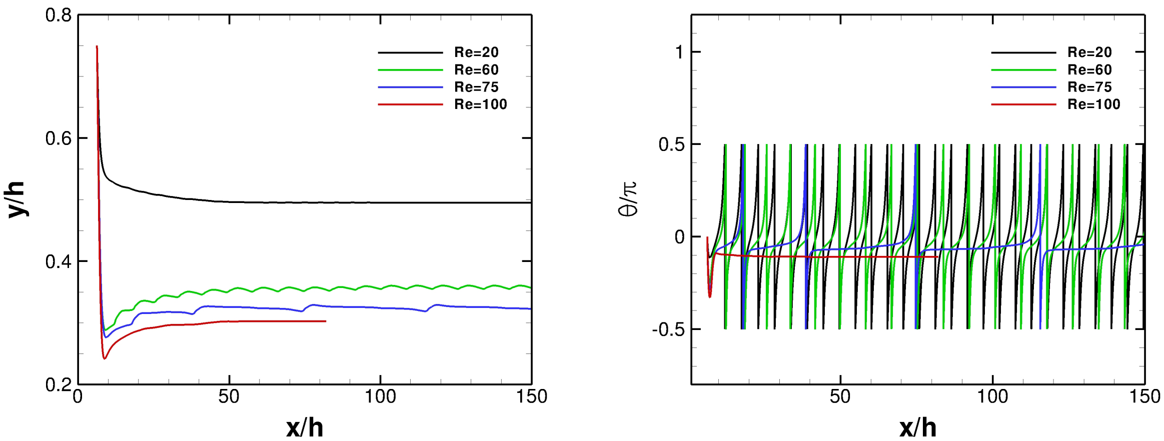

Figure 11: Vertical position (left) and angle between the major axis of the particle and the horizontal axis (right) for the ellipse released at $h_0/h = 0.75$, at different Reynolds numbers.

that depends on the type of flow, independently of their initial positions. Elliptic and triangular particles reach the equilibrium position showing a periodic behavior around a mean value. For the Couette flow, the particles travel with the same undisturbed fluid velocity corresponding to their vertical position, and rotate with angular velocity very close to the constant one of the undisturbed flow. For the Poiseuille flow, the particles migrate to an equilibrium position between the wall and the middle of the channel, and always lag the local velocity of the undisturbed flow. Finally, the influence of increasing the Reynolds number (Re) on the motion of the elliptic particle is studied in some detail: the time-averaged equilibrium position moves toward the wall as Re increases. For small Res, the angular velocity of the particle is periodic in time and reaches its maximum value through spikes. With increasing Re, the rotation period increases and eventually rotation subsides, the particle remaining with its major axis almost oriented along the flow direction. In this paper, only two-dimensional particles have been considered to test the methodology, although it is fully three-dimensional. The method is very efficient and will be used as a very useful tool to understand the fluid mechanics controlling the side forces, the turning moments and the effects of the wall on the migration and the equilibrium position of the particles. Finally, particle-particle and particle-wall collision models will be implemented, in order to enable the proposed methodology to investigate the transport of multiple bodies.

References

[1] D. Qi, L. Luo, R. Aravamuthan, and W. Strieder. Lateral migration and orientation of elliptical particles in Poiseuille flows. *Journal of Statistical Physics*, 107:101–120, 2002.

[2] S.Y. Lee, M. Ferrari, and Decuzzi P. Shaping nano-/micro-particles for enhanced vascular interaction in laminar flows. *Nanotechnology*, 20:495191, 2009.

[3] G. Adriani, M.D. de Tullio, M. Ferrari, F. Hussain, G. Pascazio, X. Liu, and P. Decuzzi. The preferential targeting of the diseased microvasculature by disk-like particles. *Biomaterials*, 33:5504–5513, 2012.

[4] C. S. Peskin. Flow patterns around heart valves: A numerical method. *J. Comput. Phys.*, 10:252, 1972.

[5] R. Mittal and G. Iaccarino. Immersed boundary methods. *Annu. Rev. Fluid Mech.*, 37:239, 2005.

[6] E. A. Fadlun, R. Verzicco, P. Orlandi, and J. Mohd-Yosuf. Combined immersed-boundary finite-difference methods for three-dimensional complex flow simulations. *J. Comput. Phys.*, 161:35, 2000.

[7] P. De Palma, M. de Tullio, G. Pascazio, and M. Napolitano. An immersed boundary method for compressible viscous flows. *Comput. Fluids*, 35:693, 2006.

[8] M.D. de Tullio, P. De Palma, G. Iaccarino, G. Pascazio, and M. Napolitano. An immersed boundary method for compressible flows using local grid refinement. *Journal of Computational Physics*, 225:2098–2117, 2007.

[9] M. Uhlmann. An immersed boundary method with direct forcing for the simulation of particulate flows. *Journal of Computational Physics*, 209:448–476, 2005.

[10] J. Yang and E. Balaras. An embeeded-boundary formulation for large-eddy simulation of turbulent flows interacting with moving boundaries. *Journal of Computational Physics*, 215:12–40, 2006.

[11] M. Vanella and E. Balaras. A moving-least-squares reconstruction for embedded-boundary formulations. *Journal of Computational Physics*, 228:6617–6628, 2009.

[12] R. Verzicco and P. Orlandi. A fiinite difference scheme for three-dimensional incompressible flows in cylindrical coordinates. *Journal of Computational Physics*, 123:402–413, 1996.

[13] N. Swartzrauber, P. A direct method for the discrete solution of separable elliptic equations. *SIAM J. Numer. Anal.*, 11:1136–1150, 1974.

[14] M.D. de Tullio, A. Cristallo, E. Balaras, and R. Verzicco. Direct numerical simulation of the pulsatile flow through an aortic bileaflet mechanical heart valve. *Journal of Fluid Mechanics*, 622:259–290, 2009.

[15] Coutanceau M. and Bouard R. Experimental determination of the main features of the viscous flow in the wake of a circular cylinder in uniform translation. Part 1. Steady flow. *J. Fluid Mech.*, 79:231–256, 1977.

[16] Tritton D.J. Experiments on the flow past a circular cylinder at low Reynolds number. *J. Fluid Mech.*, 6:547–567, 1959.

[17] Linnick M.N. and Fasel H.F. A high-order immersed boundary method for unsteady incompressible flow calculations. *41st AIAA Aerospace Sciences Meeting and Exhibit*, Reno, NV, 2003.

[18] K. Taira and T. Colonius. The immersed boundary method: a projection approach. *Journal of Computational Physics*, 225:2118–2137, 2007.

[19] Berger E. and Willie R. Periodic flow phenomena. *Ann. Rev. Fluid Mech.*, 4:313–340, 1972.

[20] D.V. Le, B.C. Khoo, and J. Peraire. An immersed interface method for viscous incompressible flows involving rigid and flexible boundaries. *Journal of Computational Physics*, 220:109–138, 2006.

[21] E. Guilmineau and P. Queutey. A numerical simulation of vortex shedding from an oscillating circular cylinder. *Journal of Fluids and Structures*, 16:773–794, 2002.

[22] Z. Xia, K.W. Connington, S. Rapaka, P. Yue, Feng J.J., and S. Chen. Flow patterns in the sedimentation of an elliptical particle. *Journal of Fluid Mechanics*, 625:249–272, 2009.

[23] A. ten Cate, C.H. Nieuwstad, J.J. Derksen, and Van den Akker H.E.A. Particle imaging velocimetry experiments and lattice-boltzmann simulations on a single sphere settling under gravity. *Physics of Fluids*, 14:4012–4025, 2002.

[24] F. Abraham. Functional dependence of drag coefficient of a sphere on Reynolds number. *Physics of Fluids*, 13:2194, 1970.

[25] J. Feng, H.H. Hu, and D.D. Joseph. Direct simulation of initial value problem for the motion of solid bodies in a Newtonian fluid. Part 1. Sedimentation. *Journal of Fluid Mechanics*, 261:95, 1994.

[26] J. Feng, H.H. Hu, and D.D. Joseph. Direct simulation of initial value problem for the motion of solid bodies in a Newtonian fluid. Part 2. Couette and Poiseuille flows. *Journal of Fluid Mechanics*, 277:271–301, 1994.

[27] B.P. Ho and G. Leal. Inertial migration of rigid spheres in two-dimensional unidirectional flows. *Journal of Fluid Mechanics*, 65:365–400, 1974.

[28] P. Vasseur and R.G. Cox. The lateral migration of a spherical particle in two-dimensional shear flows. *Journal of Fluid Mechanics*, 78:385–413, 1976.

[29] J.S. Halow and G.B. Wills. Experimental observations of sphere migration in Couette systems. *Industrial & Engineering Chemistry Fundamentals*, 9:603, 1970.

[30] G. Segré and A. Silberberg. Radial Poiseuille flow of suspensions. *Nature*, 189:209, 1961.

[31] G. Segré and A. Silberberg. Behaviour of macroscopic rigid spheres in Poiseuille flow. Part 1. *Journal of Fluid Mechanics*, 14:115, 1962.

[32] H.L. Goldsmith and S.G. Mason. *The microrheology of dispersions. In Rheology, Theory and Applications*, volume 4, page 85. F.R. Eirich, Academic, 1966.

[33] H. Brenner. Hydrodynamic resistance of particles at small Reynolds numbers. *Advances in Chemical Engineering*, 6:287, 1966.